

See discussions, stats, and author profiles for this publication at: <https://www.researchgate.net/publication/26858539>

# Experimental-Computational Investigation of ZnO nanowires Strength and Fracture

ARTICLE *in* NANO LETTERS · SEPTEMBER 2009

Impact Factor: 13.59 · DOI: 10.1021/nl9023885 · Source: PubMed

---

CITATIONS

117

READS

42

3 AUTHORS, INCLUDING:



Ravi Agrawal

Shell Technology Centre Bangalore

14 PUBLICATIONS 565 CITATIONS

[SEE PROFILE](#)



Decanini Horacio

Northwestern University

115 PUBLICATIONS 3,103 CITATIONS

[SEE PROFILE](#)

# Experimental-Computational Investigation of ZnO nanowires Strength and Fracture

Ravi Agrawal,<sup>†</sup> Bei Peng,<sup>†</sup> and Horacio D. Espinosa\*

Department of Mechanical Engineering, 2145 Sheridan Road, Northwestern University, Evanston, Illinois 60208-3111

Received July 24, 2009; Revised Manuscript Received September 14, 2009

## ABSTRACT

An experimental and computational approach is pursued to investigate the fracture mechanism of [0001] oriented zinc oxide nanowires under uniaxial tensile loading. A MEMS-based nanoscale material testing stage is used in situ a transmission electron microscope to perform tensile tests. Experiments revealed brittle fracture along (0001) cleavage plane at strains as high as 5%. The measured fracture strengths ranged from 3.33 to 9.53 GPa for 25 different nanowires with diameters varying from 20 to 512 nm. Molecular dynamic simulations, using the Buckingham potential, were used to examine failure mechanisms in nanowires with diameters up to 20 nm. Simulations revealed a stress-induced phase transformation from wurtzite phase to a body-centered tetragonal phase at ~6% strain, also reported earlier by Wang et al.<sup>1</sup> The transformation is partial in larger nanowires and the transformed nanowires fail in a brittle manner at strains as high as 17.5%. The differences between experiments and computations are discussed in the context of (i) surface defects observed in the ZnO nanowires, and (ii) instability in the loading mechanism at the initiation of transformation.

One-dimensional (1D) zinc oxide (ZnO) nanostructures have been synthesized in various morphologies like nanorods, nanowires,<sup>2</sup> nanobelts,<sup>3</sup> nanorings,<sup>4</sup> and nanohelices.<sup>5</sup> The extraordinary combination of semiconducting and electro-mechanical properties of ZnO nanostructures makes them potential building blocks for future nanodevices. For example, optoelectronic devices,<sup>2</sup> logic circuits,<sup>6</sup> and piezoelectric devices like nanogenerators,<sup>7,8</sup> nanoresonators, and electromechanically coupled nanocantilever sensors<sup>9</sup> have already been conceptualized. For reliable and optimal performance of these nanodevices, particularly the ones involving loading/unloading of the nanostructures, proper characterization of the mechanical response at the component level is crucial. However, the extremely small dimensions of 1D nanostructures impose major challenges to perform component level characterization with enough precision. In recent years, several attempts have been made to measure the mechanical properties of ZnO nanostructures using various techniques involving dynamic resonance in situ transmission electron microscopy (TEM)<sup>10–12</sup> and atomic force microscopy (AFM),<sup>13–15</sup> and nanoindentation.<sup>16</sup> These techniques involve various assumptions for interpretation of the acquired experimental data and the errors associated with each technique have resulted in a variety of results. Inconsistencies in the reported Young's modulus of ZnO NWs,

as a function of wire diameter, were previously reported by our group.<sup>17,18</sup> Table 1 summarizes the results from researchers who have reported the elastic as well as the failure properties of ZnO nanowires. It is important to point out that only Hoffman et al.<sup>19</sup> have reported the elastic modulus and the fracture strain using the same methodology. In most of the studies by the same research groups, entirely different methods have been employed to experimentally characterize elastic and fracture properties. This reinforces the fact that performing nanoscale experiments capable of simultaneously measuring loads and displacements with desired resolution is not trivial. For instance, Desai et al.<sup>20</sup> used piezoactuation to strain NWs lying across a trench with both ends of the NW fixed via electron-beam induced deposition of platinum. The strains were obtained by analysis of SEM images obtained during the in situ experiments. They reported size-dependent fracture strains, increasing from 5 to 15% as the NW diameter decreased from 480 to 220 nm. This technique was unable to simultaneously measure the applied loads; therefore, a separate microfabricated test bed<sup>20</sup> was used to characterize the elastic modulus. Likewise, Chen et al.<sup>10</sup> employed a dynamic resonance method to identify the modulus of ZnO NWs and an in situ SEM bending method,<sup>21</sup> using a nanomanipulator, to characterize the fracture properties. They reported a size-independent fracture strain in the range 4–7% by bending vertically grown NWs. Hoffman et al.<sup>19</sup> reported fracture strains of  $5 \pm 1.5\%$  by performing tensile experiments using an AFM tip mounted on a piezo-

\* To whom correspondence should be addressed. E-mail: espinosa@northwestern.edu. Phone: (847) 467-5989. Fax: (847) 491-3915.

<sup>†</sup> These authors contributed equally to this work.

**Table 1.** Summary of Elastic/Plastic Response of [0001] Oriented ZnO NWs Studied Experimentally

elastic properties			fracture properties			
method [ref]	Young's modulus (GPa)	size dependence	method [ref]	fracture strain (%)	size dependence	fracture strength (GPa)
in situ dynamic resonance <sup>10</sup>	140–220	yes	in situ SEM bending <sup>21</sup>	4–7%	no	7.7–12.1 <sup>a</sup>
AFM tension <sup>19</sup>	97 ± 18	no	AFM tension <sup>19</sup>	5 ± 1.5%	no	5.5 ± 1.4
microfabricated test bed <sup>20</sup>	21 ± 2	no	piezoactuation <sup>20</sup>	5–15%	yes	1.1–3.2 <sup>a</sup>
n-MTS <sup>17</sup>	140–162	yes	n-MTS (this work)	2.3–6.2%	no	3.35–9.53

<sup>a</sup> Fracture strengths are calculated based on average fracture strains or Young's modulus, whatever was reported in the literature.

stack. Although, Hoffman et al.<sup>19</sup> and Chen et al.<sup>21</sup> reported consistent size independent failure behavior of ZnO NWs, the elastic response reported by them were quite different. Chen et al.<sup>10</sup> observed that the Young's modulus increased from 140 to 220 GPa, as the wire diameter decreased from 550 to 17 nm. However, Hoffman et al.<sup>19</sup> reported a size independent modulus of 97 ± 18 GPa.

In addition to the variability in experimental findings, there is a gap between computational predictions and experimental observations. From molecular dynamics (MD) simulations, a stress-induced transformation from wurtzite (WZ) phase to a body-centered tetragonal (BCT) phase has been reported.<sup>1</sup> A different transformation from zinc blende (ZB) cubic phase to WZ phase has been observed in the thermal vapor deposition based growth of ZnO tetrapods,<sup>22</sup> as the crystal grows bigger. However, a stress-induced phase transformation to BCT phase, as predicted by MD simulations, has not been observed experimentally to date.

In our earlier work,<sup>17</sup> we unambiguously characterized the elastic properties of ZnO nanowires and identified size dependence using a combined experimental–computational approach. Our analysis revealed that the elastic modulus decreases from ~190 to 140 GPa, as the NW diameter increases from 5 to 80 nm. In this work, we follow a similar approach to investigate the failure behavior of ZnO NWs. We report experimental results on the failure of ZnO NWs under uniaxial tensile loading and compare them to atomistic simulations. Experiments were performed on [0001] oriented ZnO NWs ranging from 20 to 512 nm in diameter while molecular dynamic (MD) simulations were performed on NWs as large as 20 nm in diameter. The experimental and computational results are compared and observed differences are discussed from both computational and experimental perspective.

The experiments were performed using a micro-electro-mechanical system (MEMS)-based nanoscale-Material Testing System (n-MTS).<sup>23–25</sup> In the n-MTS, axial displacement is applied using the thermal actuator on one side of the mobile testing stage, and load is measured using a differential capacitive-based load sensor on the other side (Figure 1a). The protocol for mounting the NWs and conducting the tensile tests was reported elsewhere.<sup>17</sup> The main advantage of this technique is that uniaxial tension is applied to the NW in a displacement-controlled manner with the simultaneous measurement of applied loads and real time TEM imaging. Figure 1b–e shows a series of images acquired during the in situ TEM test of a ZnO NW, 55 nm in diameter. As the sample was strained, a few regions on the NW showed local bright-field contrast. At one of these regions, fracture

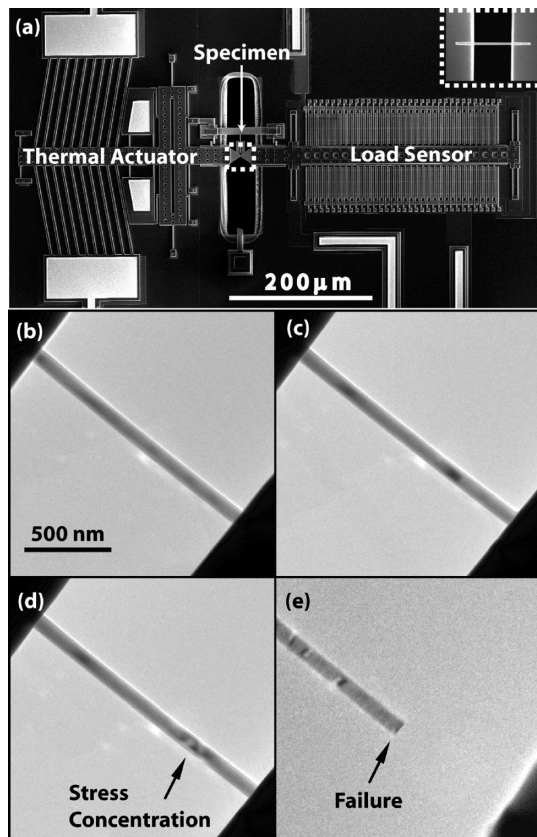


**Figure 1.** (a) SEM micrograph of the MEMS-based n-MTS (inset: a mounted NW on the test bed). (b–e) A sequence of TEM images taken during the tensile testing of ZnO NW until fracture.

occurred, Figure 1c–e. The local changes observed in contrast may be related to atomic distortions resulting from stress concentrations. Figure 1d shows the sample just before fracture and Figure 1e shows the remaining portion of the sample after fracture. Several fringes are evident in the bright-field image (Figure 1e). It is noteworthy that after fracture, one-half of the NW disappeared and failed at the weld also indicating that there might be an instability associated with failure which will be discussed later. Figure 2a shows the combined stress–strain and load–displacement plot for the NW. The stress–strain response was computed from measured loads and displacements as follows. The strains were computed using two independent methods: (i) average strain by measuring the gap, between the shuttles, from the TEM images, and (ii) local atomic strains from selected area diffraction (SAD) patterns acquired during loading (see ref 17 for further details). Average strains and local atomic strains were in good agreement, ensuring that no slippage occurred at the fixed ends of the welded NW.

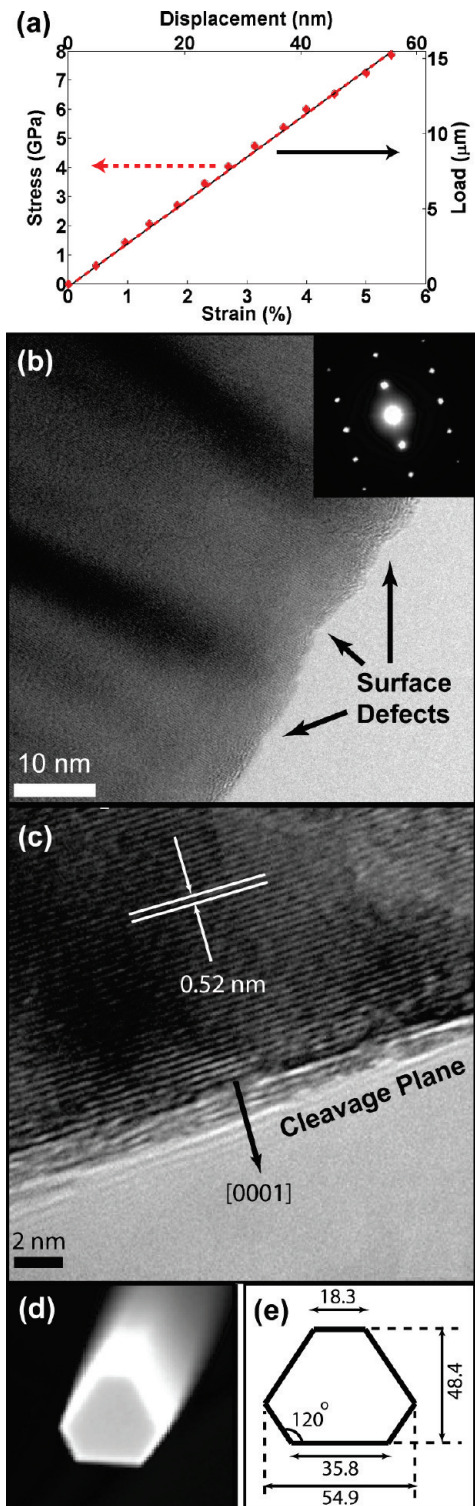


**Figure 2.** (a) Stress–strain (red dotted line) and load–displacement (black solid line) plot obtained experimentally for a 55 nm NW. (b) TEM image showing surface defects (inset: diffraction pattern conforming WZ structure and [0001] orientation. (c) HRTEM image of the cleavage plane. (d) SEM image of the fractured surface. (e) Schematic used to calculate the cross-sectional area (dimensions are in nanometers).

For measurement of stresses, the loads were calculated from the calibration of the load sensor and the cross-sectional areas were calculated by measuring the dimensions of the fractured surface from SEM images (as illustrated in Figure 2d,e). All

of these measured quantities (strains, loads, and cross-sectional area) were then used to compute the stress–strain response for each nanowire.

Figure 2b shows a TEM bright field image and the corresponding selected area diffraction pattern (inset in Figure 2b) for a ZnO NW prior to loading. The diffraction pattern was indexed based on a hexagonal wurtzite cell with lattice parameters  $a = 3.25 \text{ \AA}$  and  $c = 5.21 \text{ \AA}$ . The measured lattice fringe spacing of  $5.21 \text{ \AA}$  confirmed that the wires were [0001] oriented. The perfect crystal lattice away from the edge asserted that defects are less probable in the volume of the NW. However, the waviness at the edge revealed that some atoms were missing from the surface. These missing atoms are likely to cause stress concentrations and initiate failure. After fracture, the failed region was further analyzed at high magnification to determine the fracture cleavage plane. The HRTEM image, shown in Figure 2c, confirmed that fracture occurred along the (0001) cleavage plane. Figure 2d shows the fracture surface, which appears mirror-smooth, as expected in the case of brittle fracture. The outer equivalent diameter, the tensile strength, and the fracture strain measured for all the 25 tested samples are provided in Supporting Information. In our experiments, the elastic behavior showed size dependence.<sup>17</sup> By contrast, fracture strains did not show correlation with wire diameter. The measured fracture strains ranged from 2.4–6%, which is in agreement with the results reported by two earlier studies (see Table 1). To understand the variation in fracture strength, we applied a Weibull-type weakest-link probabilistic model to verify if the observed variation can be associated with the surface defects present in the nanowires. Classical Weibull statistics<sup>26,27</sup> assumes the probability of failure  $P_f$  for a specimen of surface area  $A$  under uniaxial stress as

$$P_f = 1 - \exp\left(-\left(\frac{\sigma_f}{\sigma_{0A}}\right)^m A\right) \quad (1)$$

where  $\sigma_f$  is the failure strength, and  $\sigma_{0A}$  is the characteristic strengths relative to unit volume or surface area respectively, and  $m$  is the Weibull modulus. The fracture strength as a function of NW surface area is plotted in Figure 3a, which shows a general trend that fracture strength of the NW increases with decreasing surface area. The classical Weibull statistics applied to this set of fracture strength data with respect to the surface area is shown in Figure 3b, where probabilities ( $P_f$ ) are calculated as

$$P_f(\sigma_i) = \frac{i - 1/2}{N} \quad (2)$$

where  $N$  is the total number of specimens tested and their observed strengths  $\sigma_1, \sigma_2, \sigma_3, \dots, \sigma_N$  are ranked in ascending order. The Weibull modulus is found to be  $m = 7.4$  and the coefficient of correlation is  $\sim 72\%$ . This indicates that fracture strength, to some extent, is associated with the surface area of the nanowires. Typically, better correlation can be achieved if the number of experiments is doubled. To further understand the experimental findings and the effect of

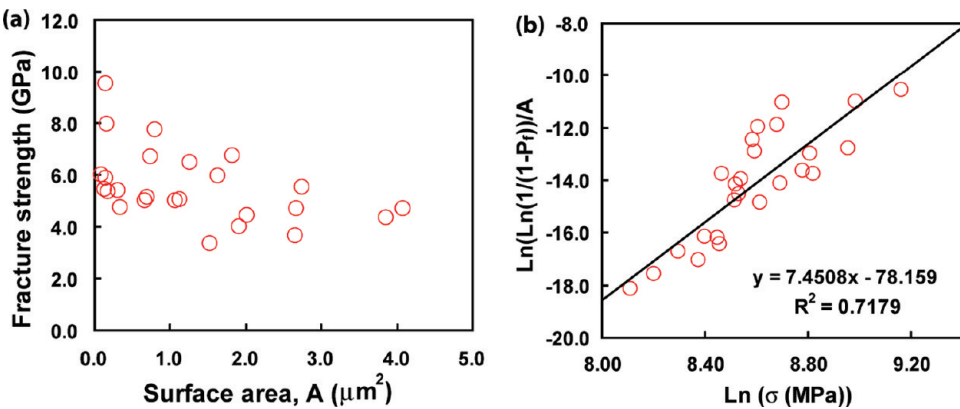


**Figure 3.** (a) Failure stress plotted vs the surface area of the nanowires. (b) Plot of the Weibull statistics.

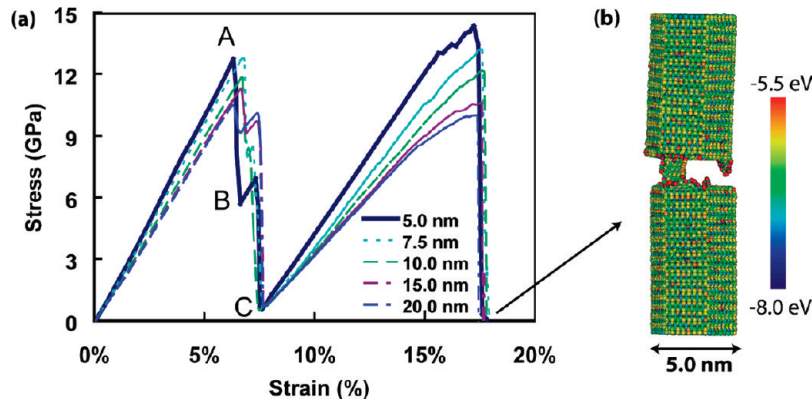


**Figure 4.** (a) Computationally obtained stress–strain response for pristine NWs ranging from 5.0 to 20.0 nm in diameter. (b) A 5.0 nm NW at 17.6% strain revealing brittle fracture of the transformed NW.

defects, computational modeling of nanowires ranging from 5 to 20 nm in diameter was performed. Simulation results are discussed next.

LAMMPS<sup>28,29</sup> (Large-Scale Atomic/Molecular Massively Parallel Simulator), developed at Sandia National Laboratories, was used to model [0001] oriented ZnO NWs with diameters ranging from 5 to 20 nm. The short-range atomic interactions were modeled with a Buckingham<sup>30</sup> type potential and long-range ionic interactions were computed based on Wolf's method.<sup>31</sup> Further details on the computational methodology can be found in ref 17. The defect-free stress–strain response obtained computationally, as a function of wire diameter, is plotted in Figure 4. Similar to the findings reported by Wang et al.,<sup>1</sup> our simulations also predict a stress-induced phase transformation from the wurtzite phase to the body-centered tetragonal phase. The onset of the transformation occurs at approximately 6.5% strain and the transformed wire loads up to ~17.5% before failing (Figure 4b) in a brittle manner. The transformation is accompanied by a dramatic stress relaxation (from A to C in the stress–strain plots, Figure 4). We observe that the transformation is not complete as reported earlier, but partial for nanowires with larger diameter. The transformation happens in two steps corresponding to two stress drops (from A to B and from B to C, Figure 4). The first drop results in the transformation of the atoms closer to [0110] surfaces. This indicates that the phase transformation initiates at the surface,

progressing toward the center as strain is further increased. To show the transformed phase, we have plotted the atomic rearrangement in one of the (2̄1̄0) planes (yz-plane, as shown schematically in Figure 5a) in the middle of the wire. Figure 5 panels b–d are snapshots of a section of (2̄1̄0) planes taken at points A and C (see Figure 4) for 5, 10, and 20 nm NWs, respectively. The shaded area reveals the 4-atom rings of the transformed BCT phase and it is evident that the larger wires retain WZ phase in some regions of the core. Analysis of the same set of atoms, prior to failure at ~17.5% strain, also reveals the same atomic arrangement confirming that no further transformation occurs in the second loading regime between 8% (point C) and 17.5% strain (failure).

Several differences between experimental and MD results, here reported, can be highlighted. (i) MD simulations predict a stress-induced phase transformation, as opposed to brittle failure (and no transformation) observed in the experiments; and (ii) the fracture strain observed in the experiments range from 2.4 to 6%, whereas the simulations predict a transformation in the range 6.5–7.5% strain followed by reloading and brittle failure at very high strains of ~17.5%. Key questions that need to be considered to analyze these differences are (i) Can surface defects account for the lower strains to fracture measured experimentally? (ii) Is the loading stage capable of following the abrupt stress drop associated to phase

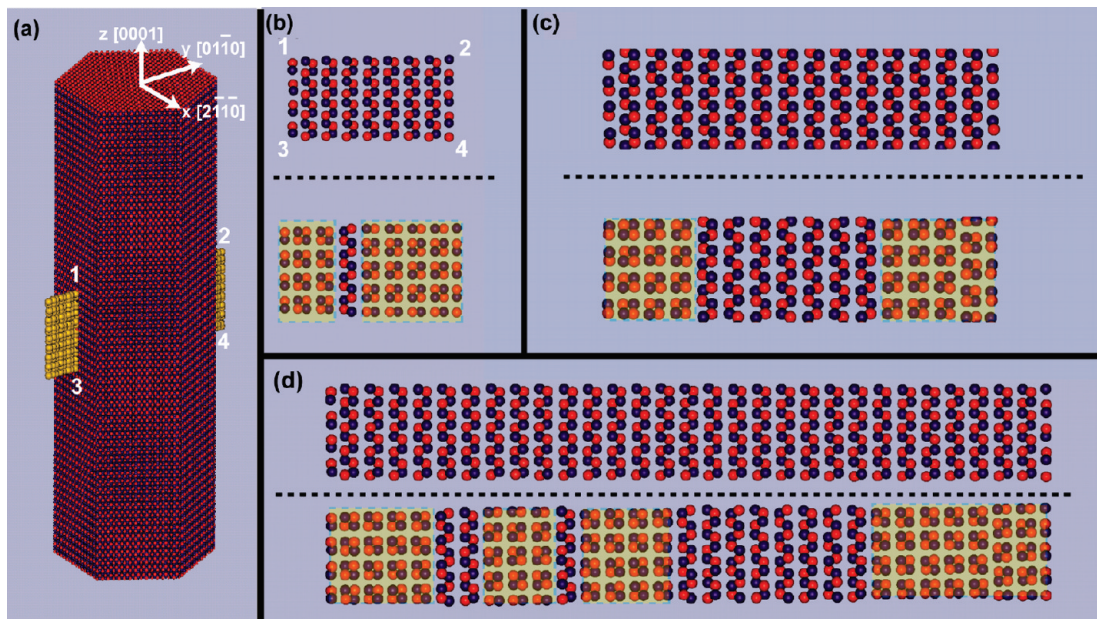


**Figure 5.** (a) An atomistic model of a NW (blue, Zn; red, O). A section of the  $yz$ -plane is schematically highlighted which is shown in (b–d) for revealing the extent of phase transformation; (b) 5 nm; (c) 10 nm; (d) 20 nm wires at points A and C of the stress–strain response. The region shaded in yellow represents the transformed BCT phase.

transformation or fracture? (iii) How accurate is the Buckingham potential in predicting fracture?

Surface defects present in experimentally tested NWs (Figure 2b) differentiate them from the pristine NWs computationally modeled. These surface defects are regions of stress concentrations that can lead to NW failure, as shown in Figure 1c–e. Moreover given that phase transformation is surface driven, it is likely to be affected by the presence of defects. Therefore, to address this we modeled nanowires with surface defects. As observed in the TEM images (Figure 2b), surface defects appear in the form of atomic waviness, which can be mathematically approximated by a sinusoidal function. Hence, the radius of the defective NW was approximated by  $R_{\text{NW}} = R + A \sin(2\pi\lambda/L)$ , where  $R$  is the nominal radius,  $L$  is the length of the NW, and  $A$  and  $\lambda$  are parameters defining the characteristics of the defect. Physically,  $A$  is representative of the size of atomic undulations observed via HRTEM and  $\lambda$  represents the density of such undulations. For  $\lambda$ , we employed a value resulting in two defects within the length of the periodic NW model. Two values of  $A$  were considered, (i)  $A = 2.5 \text{ \AA}$  (i.e., 5% of NW radius) and (ii)  $A = 5.0 \text{ \AA}$  (i.e., 10% of NW radius). These defective NWs were then annealed and strained following the same protocol as the one used for the defect-free NWs. Figure 6a shows the atomic energies after annealing for a 10 nm NW without and with defects of amplitudes 2.5 and 5  $\text{\AA}$ . Figure 6c shows the stress–strain response for the three configurations. Similar to the defect-free case, the defective NWs also revealed a two phase loading; however, the overall stresses to initiate the transformation and to initiate fracture were reduced. For the case  $A = 2.5 \text{ \AA}$ , the defect size was too small to affect the linear elastic response of the nanowire. However, for  $A = 5 \text{ \AA}$ , a small plateau was observed at  $\sim 4\%$  strain. Analysis of atomic configurations (Figure 6b) revealed that the atoms closer to (0110) surface and corresponding

to the depth of the defect get transformed in this plateau region.

These results reveal that surface defects reduce the average nucleation stresses because of stress concentrations; however, their presence did not inhibit the phase transformation completely. The stress at which transformation is predicted in the presence of defects lie in the range in which fracture was observed experimentally, that is, 3 to 9 GPa. Therefore, one would think that there might be some experimental limitation, which does not allow for the observation of the transformed phase in the experiments.

In our experimental technique, the thermal actuator is displacement controlled. However, it is important to note that for brittle materials, like ZnO, some instabilities might arise particularly when the transformation (or fracture) is about to happen. This is explained schematically in Figure 7. Figure 7a shows the initial configuration at 0% strain, where a NW of length  $L$  is mounted on the device between the thermal actuator and the load sensor. When the NW is loaded by applying a displacement  $d_a$  to the thermal actuator, the strain induced in the NW is given by,  $\epsilon = (d_a - d_s)/L$ . Here,  $d_s$  is the deflection of the load sensor shuttle due to the force transmitted through the NW ( $F_{\text{NW}}$ ). If the load sensor shuttle is suspended by the folded beams with effective stiffness,  $k$ , then the load in the NW is measured as  $F_{\text{NW}} = F_s = kd_s$ . This stable condition (Figure 7b) is maintained as long as the NW is in the elastic regime (up to point A, in Figure 4). In the event of a phase transformation, as predicted by MD simulations, there is a dramatic drop in force (or stress) in the NW (point C, in Figure 4). This implies that the force transmitted to the load sensor,  $F_s$ , drops almost to zero. As a result,  $d_s$  also tends to zero suddenly bringing the load sensor shuttle to its initial configuration (c). Therefore, a quasi-static compatible deformation in the NW does not occur and unloading waves are generated. We

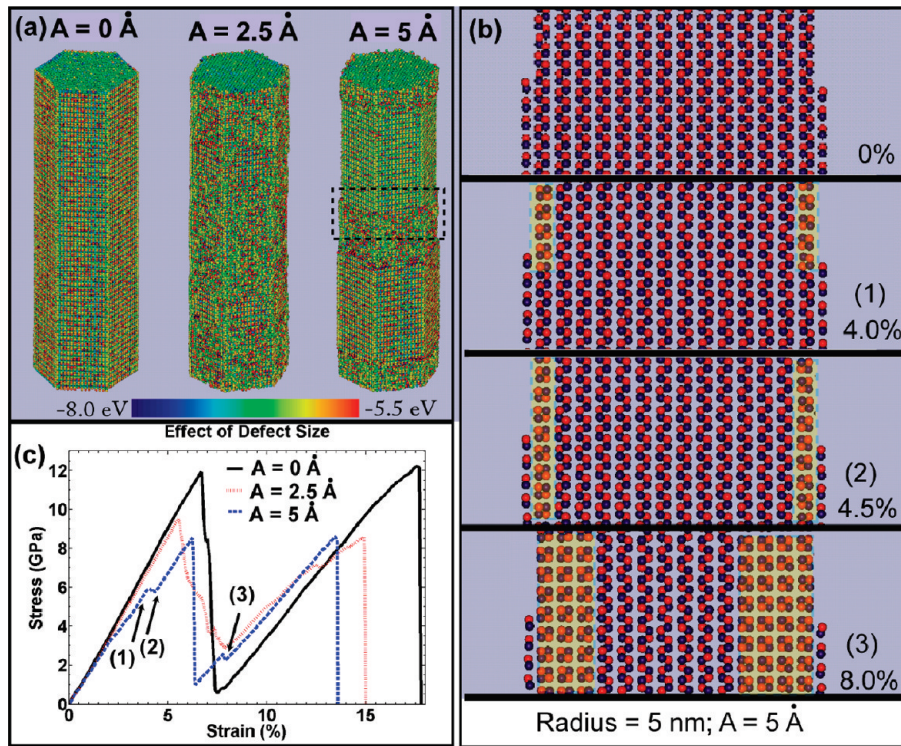


**Figure 6.** (a) Three configurations of 10 nm diameter NW with increasing defect size after annealing. Atomic energies are plotted. (b) A section of yz-plane shown at increasing strains to reveal the transformation process. (c) Stress–strain response for the three configurations

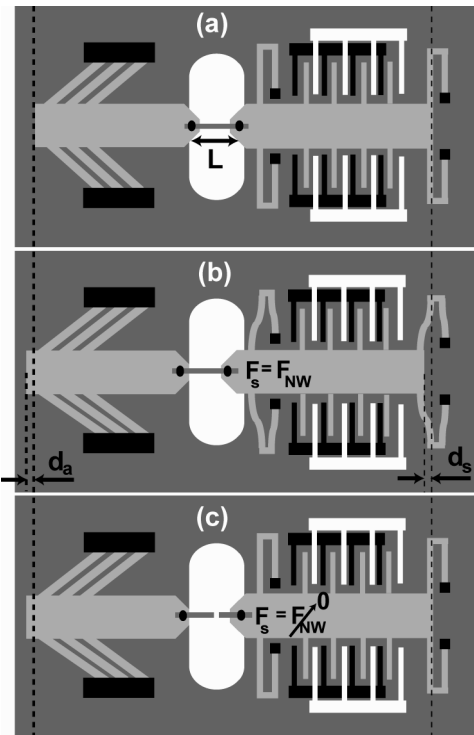


**Figure 7.** (a) Schematic of the n-MTS showing initial configuration when NW is not loaded; (b) configuration when the wire is loaded prior to transformation or failure – forces are balanced; (c) at the point of transformation (or failure) due to sudden stress relaxation (or drop in force), the load sensor relapses whereas thermal actuator retains its earlier position resulting in a very high strain.

hypothesize that the dynamics of the load sensor generates unloading stress waves in the NW leading to its fracture.

This necessitates the development of an improved electro-mechanical system capable of maintaining quasi-static loading conditions throughout the tensile test.

In addition to this experimental limitation, the validity of the Buckingham potential in predicting phase transition and fracture needs to be assessed by means of first principle calculations. The two-body pairwise nature of Buckingham type potential might not be precise enough to capture the complex phenomena of fracture (or phase transformation), which involves bond rotation, bond breaking, and bond formation. Earlier, first principle studies using density functional theory (DFT) performed on bulk crystals calculated the enthalpy of WZ and BCT phases as a function of applied stresses.<sup>32</sup> It was revealed that BCT phase has lower energy beyond certain stress and therefore, a likelihood of the transformation was asserted. However, these earlier studies had two major limitations, (i) the surface effect was not modeled, which is relevant in case of nanowires, particularly, because MD reveals that the transformation initiates at the surface, and (ii) the enthalpy of BCT phase was shown to be lower as compared to WZ phase beyond certain stresses, but an energy barrier was never calculated to confirm that the phase transformation is energetically feasible. Preliminary DFT calculations performed on defect-free NWs, with periodicity and a length of 2 unit cells, suggest that the NWs can be deformed elastically to strains as high as 20%. The DFT reveals similar WZ–BCT phase transformation, but only prior to fracture. The effects of unit cell size and surface atomic defects (waviness) on the DFT predictions need to be assessed. These issues are under investigation and will be discussed in a future publication.<sup>33</sup>

In summary, this work has experimentally identified the fracture properties of ZnO NWs in uniaxial tension. Fracture stresses as high as 9.53 GPa and failure strains of 6.2% were measured. These strains are about 5 times those exhibited by the material in bulk or thin film form. This finding highlights the advantage of using NWs in piezoelectric nanodevices because voltage induced by mechanical deformation is proportional to the maximum achievable strain. MD simulations with the Buckingham potential revealed that surface defects can significantly lower the maximum average stress prior to failure. A major drop in stress is also predicted at strains of  $\sim$ 6.5%, which is consistent with the experimental findings. However, the MD simulations predict a phase transformation, which has not been observed experimentally. This motivates the need for developing more advanced experimental protocols to avoid instabilities and for the use of DFT-based quantum mechanical studies to verify the predictive capabilities of the Buckingham potential.

**Acknowledgment.** This work was supported by the National Science Foundation under Award Number CMMI-0555734 and EEC-0647560. The authors acknowledge usage of the Electron Probe Instrumentation Center facilities at Northwestern University. The authors also acknowledge the use of resources of the Argonne Leadership Computing Facility at Argonne National Laboratory, which is supported by the Office of Science of the U.S. Department of Energy under contract DE-AC02-06CH11357. We thank I. Petrov and E. Olson for their contribution in the development of in situ TEM holder. We thank Dr. Shuyou Li for helping us with TEM imaging and diffraction analyses. We also acknowledge Dr. Michael Baskes from Los Alamos National Laboratories and Dr. S. G. Srivilliputhur from the University of North Texas for insightful discussions. We also thank an undergraduate student, Eleftherios Gdoutos, for helping with postprocessing of the computational data.

**Supporting Information Available:** Table S1 summarizes the dimensions and fracture properties of all the nanowires tested experimentally. This material is available free of charge via the Internet at <http://pubs.acs.org>.

## References

- (1) Wang, J.; Kulkarni, A. J.; Ke, F. J.; Bai, Y. L.; Zhou, M. Novel mechanical behavior of ZnO nanorods. *Comput. Meth. Appl. Mech. Eng.* **2008**, *197*, 3182–3189.
- (2) Huang, M. H.; Mao, S.; Feick, H.; Yan, H.; Wu, Y.; Kind, H.; Weber, E.; Russo, R.; Yang, P. Room-temperature ultraviolet nanowire nanolasers. *Science* **20018**, 1897–1899.
- (3) Pan, Z. W.; Dai, Z. R.; Wang, Z. L. Nanobelts of semiconducting oxides. *Science* **2001**, *291*, 1947–1949.
- (4) Kong, X. Y.; Ding, Y.; Yang, R.; Wang, Z. L. Single-crystal nanorings formed by epitaxial self-coiling of polar nanobelts. *Science* **2004**, *303*, 1348–1351.
- (5) Gao, P. X.; Ding, Y.; Mai, W.; Hughes, W. L.; Lao, C. S.; Wang, Z. L. Conversion of zinc oxide nanobelts into superlattice-structured nanohelices. *Science* **2005**, *309*, 1700–1704.
- (6) Gudiksen, M. K.; Lauhon, L. J.; Wang, J.; Smith, D. C.; Lieber, C. M. Growth of nanowire superlattice structures for nanoscale photonics and electronics. *Nature* **2002**, *415*, 617–619.
- (7) Wang, Z. L.; Song, J. Piezoelectric nanogenerators based on zinc oxide nanowire arrays. *Science* **2006**, *312*, 242.
- (8) Gao, P. X.; Song, J.; Liu, J.; Wang, Z. L. Nanowire piezoelectric nanogenerators on plastic substrates as flexible power sources for nanodevices. *Adv. Mater.* **2007**, *19*, 67–72.
- (9) Cui, Y.; Wei, Q.; Park, H.; Lieber, C. M. Nanowire nanosensors for highly sensitive and selective detection of biological and chemical species. *Science* **2001**, *293*, 1289–1291.
- (10) Chen, C. Q.; Shi, Y.; Zhang, Y. S.; Zhu, J.; Yan, Y. J. Size dependence of young's modulus in ZnO nanowires. *Phys. Rev. Lett.* **2006**, *96*, 075505.
- (11) Huang, Y.; Bai, X.; Zhang, Y. In situ mechanical properties of individual ZnO nanowires and the mass measurement of nanoparticles. *J. Phys.: Condens. Matter* **2006**, *18*, L179–L184.
- (12) Bai, X. D.; Gao, P. X.; Wang, Z. L.; Wang, E. G. Dual-mode mechanical resonance of individual ZnO nanobelts. *Appl. Phys. Lett.* **2003**, *82* (26), 4806–4808.
- (13) Stan, G.; Ciobanu, C. V.; Parthangal, P. M.; Cook, R. F. Diameter-dependent radial and tangential elastic moduli of ZnO nanowires. *Nano Lett.* **2007**.
- (14) Song, J.; Wang, X.; Riedo, E.; Wang, Z. L. Elastic property of vertically aligned nanowires. *Nano Lett.* **2005**, *5* (10), 1954–1958.
- (15) Ni, H.; Li, X. Young's modulus of ZnO nanobelts measured using atomic force microscopy and nanoindentation techniques. *Nanotechnology* **2006**, *17*, 3591–3597.
- (16) Ji, L. W.; Young, S. J.; Fang, T. H.; Liu, C. H. Buckling characterization of vertical ZnO nanowires using nanoindentation. *Appl. Phys. Lett.* **2007**, *90*, 033109.
- (17) Agrawal, R.; Peng, B.; Gdoutos, E. E.; Espinosa, H. D. Elasticity size effects in ZnO nanowires - a combined experimental-computational approach. *Nano Lett.* **2008**, *8* (11), 3668–3674.
- (18) Park, H. S.; Cai, W.; Espinosa, H. D.; Huang, H. Mechanics of crystalline nanowires. *MRS Bull.* **2009**, *34* (3), 178–183.
- (19) Hoffmann, S.; Orlund, F.; Michler, J.; Fan, H. J.; Zacharias, M.; Christiansen, S. H.; Ballif, C. Fracture strength and young's modulus of ZnO nanowires. *Nanotechnology* **2007**, *18*, 205503.
- (20) Desai, A. V.; Haque, M. A. Mechanical properties of ZnO nanowires. *Sens. Actuators A* **2006**.
- (21) Chen, C. Q.; Zhuo, J. Bending strength and flexibility of ZnO nanowires. *Appl. Phys. Lett.* **2007**, *90*, 043105.
- (22) Yong, D.; Zhong, W.; Lin, Tianjun, S.; Jieshan, Q. Zinc-blende ZnO and its role in nucleating wurtzite tetrapods and twinned nanowires. *Appl. Phys. Lett.* **2007**, *90* (15), 153510.
- (23) Zhu, Y.; Corigliano, A.; Espinosa, H. D. A thermal actuator for nanoscale in-situ microscopy testing: Design and characterization. *J. Micromech. Microeng.* **2006**, *16*, 242–253.
- (24) Espinosa, H. D.; Zhu, Y.; Moldovan, N. Design and operation of a mems-based material testing system for nanomechanical characterization. *J. Microelectromech. Syst.* **2007**, *16* (5), 1219–1231.
- (25) Zhu, Y.; Espinosa, H. D. An electromechanical material testing system for in situ electron microscopy and applications. *Proc. Natl. Acad. Sci. U.S.A.* **2005**, *102* (41), 14503–14508.
- (26) Weibull, W. A statistical theory of the strength of materials. *Proc. R. Swedish Inst. Eng. Res.* **1939**, *151*, 1–45.
- (27) Weibull, W. A statistical distribution function of wide applicability. *J. Appl. Mech.* **1951**, *18*, 293–297.
- (28) Plimpton, S. J. Fast parallel algorithms for short-range molecular dynamics. *J. Comput. Phys.* **1995**, *117*, 1–19.
- (29) <http://lamps.sandia.gov> (accessed September 18, 2009).
- (30) Binks, D. J. Computational modeling of zinc oxide and related oxide ceramics. In *Department of Chemistry*; University of Surrey: Harwell, 1994.
- (31) Wolf, D.; Kebbinski, P.; Phillipot, S. R.; Eggebrecht, J. Exact method for the simulation of coulombic systems by spherically truncated pairwise  $r^{-1}$  summation. *J. Chem. Phys.* **1999**, *110*, 8254.
- (32) Wang, J.; Kulkarni, A. J.; Sarasamak, K.; Limpijumpong, S.; Ke, F. J.; Zhou, M. Molecular dynamics and density functional studies of a body-centered-tetragonal polymorph of ZnO. *Phys. Rev. B* **2007**, *76* (17), 172103 (4).
- (33) Agrawal, R.; Paci, J. T. Espinosa, H. D. First principles study of fracture mechanism in ZnO nanowires. To be submitted for publication.

NL9023885